An effective high-order five-point stencil, based on integrated-RBF approximations, for the first biharmonic equation and its applications in fluid dynamics

Submitted to *International Journal of Numerical Methods for Heat & Fluid Flow*, November 2022; revised, January 2023; revised (2), February 2023; revised (3), March 2023

Abstract

Purpose - The purpose of this paper is to present a new discretisation scheme, based on equation-coupled approach and high-order five-point integrated-RBF approximations, for solving the first biharmonic equation, and its applications in fluid dynamics.

Design/methodology/approach - The first biharmonic equation, which can be defined in a rectangular or non-rectangular domain, is replaced by two Poisson equations. The field variables are approximated on overlapping local regions of only five grid points, where the integrated-RBF approximations are constructed to include nodal values of not only the field variables but also their second-order derivatives and higher-order ones along the grid lines. In computing the Dirichlet boundary condition for an intermediate variable, the integration constants are utilised to incorporate the boundary values of the first-order derivative into the boundary IRBF approximation.

Findings - These proposed IRBF approximations on the stencil and on the boundary enable the boundary values of the derivative to be exactly imposed, and the IRBF solution to be much more accurate and not influenced much by the RBF width. The error is reduced at a rate that is much greater than four. In fluid-dynamics applications, the method is able to

capture well the structure of steady highly nonlinear fluid flows using relatively coarse grids.

Originality: The main contribution of this study lies in the development of an effective high-order five-point stencil based on integrated RBFs for solving the first biharmonic equation in a coupled set of two Poisson equations. A fast rate of convergence (up to 11) is achieved.

Keywords: first biharmonic equation, coupled-equation approach, compact stencils, integrated radial basis functions, fluid flows

1 Introduction

The first biharmonic equations arise in fluid mechanics and solid mechanics. This kind of equations, where the variable and its first-order normal derivative are given along the boundary, can be solved by the non-coupled approach and the coupled-equation approach (Gupta and Manohar, 1984). For the non-coupled approach, there is only one dependent variable and thus one needs to solve one resultant set of algebraic equations. In the context of finite-difference methods, various types of stencils were developed, including the classical 13-point formula with truncation error of order h^2, i.e. $O(h^2)$ (Gupta and Manohar, 1984), 25-point formula ($O(h^4)$) (Collatz, 1960) and the compact 9-point formula ($O(h^4)$) (Stephenson, 1984). For the classical 13-point and 25-point stencils, the approximations at grid points near the boundary need to include points outside of the domain of interest, and these fictitious points are used for the purpose of incorporating the boundary conditions (Gupta and Manohar, 1984). The inclusion of fictitious points can be avoided by means of compact approximations (e.g. Stephenson, 1984; Dehghan and Mohebbi, 2006). For the compact 9-point stencil (Stephenson, 1984), the first derivatives of the solution in the x and y directions are also considered as unknowns, resulting in a much larger system of algebraic equations. In (Mai-Duy *et al.*, 2022b), the compact 9-point stencil, based on IRBF approximations, was presented for the solution of the first biharmonic problem using the non-coupled approach. Like the compact 9-point stencil in (Stephenson, 1984), there are no fictitious points involved. However, the error of the IRBF solution is reduced at the rate

that is much greater than 4.

For the equation-coupled approach, the biharmonic equation is reduced to a coupled set of two Poisson equations. One only has to deal with second-order derivatives, but needs to solve two resultant sets of algebraic equations. The main difficulty of this approach is that the boundary condition for an intermediate variable is unknown, and there is the need for using an iterative procedure to solve the two resulting coupled algebraic systems. In the context of finite-difference methods, the classical 5-point stencil, which is a second-order accurate scheme, and the compact 5-point stencil (Hirsh, 1975), which is a fourth-order accurate scheme, are typically employed to solve Poisson equations. Effort has been spent to derive classes of boundary approximations for the boundary condition of a new variable, and classes of direct and iterative schemes for solving the two resulting algebraic systems (Roache, 1998).

Radial basis functions (RBFs) have achieved remarkable success in representing functions and solving partial differential equations (PDEs). The multiquadratic function and some other types of RBFs yield spectral accuracy for interpolation and derivative approximations. The RBF approximations can be constructed through differentiation (DRBF) or integration (IRBF). The governing equations of fluid dynamics have been successfully solved by the DRBF- and IRBF-based methods (e.g. Mai-Duy and Tanner, 2005,2007; Dehghan and Shokri, 2008; Kosec and Šarler, 2008,2013; Mohebbi *et al.*, 2014; Ngo-Cong *et al.*, 2017; Ebrahimijahan and Dehghan, 2021; Ebrahimijahan *et al.*, 2020,2022,2022b; Abbaszadeh *et al.*, 2022; Mesgarani *et al.*, 2022).

This paper presents a new 5-point stencil, based on high-order IRBF approximations, for the solution of the first biharmonic problem using the coupled-equation approach, and its applications in fluid dynamics. The stencil requires only 5 grid points over which the construction of IRBF approximations is based on the 3-point approximations which have been recently developed in (Mai-Duy and Strunin, 2021; Mai-Duy *et al.*, 2022) for solving second-order PDEs. For each dependent variable, the coefficients of the interpolation in the physical space are expressed in terms of not only the nodal values of the variable but also the nodal

values of its derivatives of second order and higher ones along the grid lines. The inclusion of nodal values of high-order derivatives enables the solution accuracy to be enhanced and not affected much by the RBF width, which helps overcome the issue of finding the optimal RBF width. In computing the Dirichlet boundary condition for an intermediate variable, the integration constants are utilised to incorporate the boundary values of the first derivative into the boundary IRBF approximation. If the boundary is not a horizontal/vertical line, the IRBF approximation at a boundary node is constructed to include only the second derivative with respect to the coordinate along the associated grid line. This kind of treatment enables the boundary values of the derivative to be exactly imposed.

The remainder of the paper is organised as follows. Section 2 is a brief review of the governing biharmonic equation. The proposed method is presented in section 3. In section 4, numerical verification is carried out, where some test problems with analytic solutions and some complex fluid flows, which are defined on rectangular and non-rectangular domains, are considered. Section 5 gives some concluding remarks.

2 Governing equations

Consider the Dirichlet problem for the biharmonic equation

$$\frac{\partial^4 u}{\partial x^4} + 2\frac{\partial^4 u}{\partial x^2 \partial y^2} + \frac{\partial^4 u}{\partial y^4} = b(x,y), \quad (x,y) \in \Omega, \tag{1}$$

$$u = g_1(x,y), \quad (x,y) \in \partial\Omega, \tag{2}$$

$$\frac{\partial u}{\partial n} = g_2(x,y), \quad (x,y) \in \partial\Omega, \tag{3}$$

where Ω is a closed domain in two dimensions, $\partial\Omega$ is its boundary, $\partial u/\partial n$ represents the outward normal on $\partial\Omega$, and $b(x,y)$, $g_1(x,y)$ and $g_2(x,y)$ are some given functions.

Equation (1) is frequently split into two coupled Poisson equations

$$\frac{\partial^2 u}{\partial x^2} + \frac{\partial^2 u}{\partial y^2} = v, \tag{4}$$

$$\frac{\partial^2 v}{\partial x^2} + \frac{\partial^2 v}{\partial y^2} = b. \tag{5}$$

In this work, we are also interested in the solution of the Navier-Stokes equations within the stream function and vorticity formulation. The steady motion of a viscous incompressible fluid is governed by the following dimensionless PDEs (Roache, 1998)

$$\frac{\partial^2 \psi}{\partial x^2} + \frac{\partial^2 \psi}{\partial y^2} = \omega, \tag{6}$$

$$\frac{1}{Re}\left(\frac{\partial^2 \omega}{\partial x^2} + \frac{\partial^2 \omega}{\partial y^2}\right) = v_x \frac{\partial \omega}{\partial x} + v_y \frac{\partial \omega}{\partial y}, \tag{7}$$

where ψ is the stream function, ω the vorticity, Re the Reynolds number, and (v_x, v_y) the x and y components of the velocity vector

$$v_x = \frac{\partial \psi}{\partial y} \quad \text{and} \quad v_y = -\frac{\partial \psi}{\partial x}. \tag{8}$$

The prescribed velocities on the boundary lead to two boundary conditions for the stream function and zero for the vorticity

$$\psi = g_1(x, y), \quad (x, y) \in \partial\Omega, \tag{9}$$

$$\frac{\partial \psi}{\partial n} = g_2(x, y), \quad (x, y) \in \partial\Omega. \tag{10}$$

It is noted that our present study and previous one (Mai-Duy *et al.*, 2022b) are all concerned with numerically solving the first biharmonic equation, where Cartesian grids are used to represent the problem domain, and the discretisations are based on one-dimensional 3-point IRBF approximations. In (Mai-Duy *et al.*, 2022b), the first biharmonic equation is solved in its original form (i.e. equation (1)) with the focuses being the discretisation of fourth-order derivatives and cross/mixed derivatives, and the imposition of double boundary conditions. In this study, the first biharmonic equation is replaced by two Poisson equations (i.e. (4) and

(5) (or (6) and (7))) with the focuses being the discretisation of second-order derivatives, the process of deriving the boundary values for v (or ω) from the discretised form of equation (4) (or equation (6)) and the boundary condition (3) (or (10)), and the iterative process of solving the two resulting algebraic systems. The system matrices are constructed from the proposed compact 5-point stencils, where extra information includes the nodal values of the second derivatives and higher ones along the grid lines. Unlike the non-coupled approach reported in (Mai-Duy *et al.*, 2022b), the first-order derivatives of the variable u with respect to x and y are not included in the IRBF approximations on the proposed 5-point stencil. There are two types of IRBF approximations used in the proposed method, namely the IRBF approximations on the 5-point stencils and the one-dimensional IRBF approximations on the grid lines.

3 Proposed method

3.1 IRBF approximations on the five-point stencil

The construction of the proposed 5-point stencil is based on the one-dimensional 3-point IRBF approximations (Mai-Duy and Strunin, 2021).

3.1.1 Three-point approximations

We use η to denote the independent variables x and y, and f the dependent variables u and v. Let IRBFq (q: even number) be an IRBF scheme of order q, in which the RBFs are integrated q times. For IRBFq, there are q integration constants and one can utilise them to add q extra equations to the conversion of the RBF space into the physical space (called the conversion system). For the approximation on a set of 3 grid points $(\eta_{i-1}, \eta_i, \eta_{i+1})$, we employ these extra equations to impose derivatives of f at η_{i-1} and η_{i+1}. The second-order derivative of f at η_i is thus expressed in terms of f at $(\eta_{i-1}, \eta_i, \eta_{i+1})$ and its derivatives at

(η_{i-1}, η_{i+1})

$$\frac{\partial^2 f_i}{\partial \eta^2} = \mathcal{D}_{2\eta}^{[q]} \widehat{f}, \tag{11}$$

where $\mathcal{D}_{2\eta}^{[q]}$ is a row matrix of $(3+q)$ known coefficients and

$$\widehat{f} = \left(f_{i-1}, f_i, f_{i+1}, \frac{\partial^2 f_{i-1}}{\partial \eta^2}, \frac{\partial^2 f_{i+1}}{\partial \eta^2} \right)^T,$$

for $q = 2$, and

$$\widehat{f} = \left(f_{i-1}, f_i, f_{i+1}, \frac{\partial^2 f_{i-1}}{\partial \eta^2}, \frac{\partial^2 f_{i+1}}{\partial \eta^2}, \ldots, \frac{\partial^{q/2+1} f_{i-1}}{\partial \eta^{q/2+1}}, \frac{\partial^{q/2+1} f_{i+1}}{\partial \eta^{q/2+1}} \right)^T,$$

for $q \geq 4$. Further details can be found in (Mai-Duy and Strunin, 2021).

3.1.2 Five-point stencil

The proposed discretisation is based on 5-point stencils. A stencil consists of the central point and the four neighbouring nodes, which are denoted by 1-5 (Figure 1). We apply point collocation to discretise the Poisson equations (4) and (5). At the central node of each stencil, one has

$$\frac{\partial^2 f_3}{\partial x^2} + \frac{\partial^2 f_3}{\partial y^2} = F_3, \tag{12}$$

where F_3 becomes v_3 when the Poisson equation is (4) and b_3 when the Poisson equation is (5).

Using (11), the second-order derivative of f with respect to x is expressed as

$$\begin{aligned} \frac{\partial^2 f_3}{\partial x^2} = {} & \mathcal{D}_{2x}^{[q]}(1) f_1 + \mathcal{D}_{2x}^{[q]}(2) f_3 + \mathcal{D}_{2x}^{[q]}(3) f_5 + \\ & \mathcal{D}_{2x}^{[q]}(4) \frac{\partial^2 f_1}{\partial x^2} + \mathcal{D}_{2x}^{[q]}(5) \frac{\partial^2 f_5}{\partial x^2} + \cdots + \mathcal{D}_{2x}^{[q]}(q+2) \frac{\partial^{q/2+1} f_1}{\partial x^{q/2+1}} + \mathcal{D}_{2x}^{[q]}(q+3) \frac{\partial^{q/2+1} f_5}{\partial x^{q/2+1}}, \end{aligned} \tag{13}$$

where $\mathcal{D}_{2x}^{[q]}(k)$, $k = (1, 2, \ldots, q+3)$, is the kth element of the coefficient set $\mathcal{D}_{2x}^{[q]}$.

Let

$$R_{2x}^{[q]} = \mathcal{D}_{2x}^{[q]}(4)\frac{\partial^2 f_1}{\partial x^2} + \mathcal{D}_{2x}^{[q]}(5)\frac{\partial^2 f_5}{\partial x^2} + \cdots + \mathcal{D}_{2x}^{[q]}(q+2)\frac{\partial^{q/2+1} f_1}{\partial x^{q/2+1}} + \mathcal{D}_{2x}^{[q]}(q+3)\frac{\partial^{q/2+1} f_5}{\partial x^{q/2+1}},$$

equation (13) reduces to

$$\frac{\partial^2 f_3}{\partial x^2} = \mathcal{D}_{2x}^{[q]}(1) f_1 + \mathcal{D}_{2x}^{[q]}(2) f_3 + \mathcal{D}_{2x}^{[q]}(3) f_5 + R_{2x}^{[q]}. \tag{14}$$

In a similar way, the second-order derivative of f with respect to y is expressed as

$$\frac{\partial^2 f_3}{\partial y^2} = \mathcal{D}_{2y}^{[q]}(1) f_2 + \mathcal{D}_{2y}^{[q]}(2) f_3 + \mathcal{D}_{2y}^{[q]}(3) f_4 + R_{2y}^{[q]}, \tag{15}$$

where $\mathcal{D}_{2y}^{[q]}(k)$, $k = (1, 2, \ldots, q+3)$, is the kth element of the coefficient set $\mathcal{D}_{2y}^{[q]}$, and

$$R_{2y}^{[q]} = \mathcal{D}_{2y}^{[q]}(4)\frac{\partial^2 f_2}{\partial y^2} + \mathcal{D}_{2y}^{[q]}(5)\frac{\partial^2 f_4}{\partial y^2} + \cdots + \mathcal{D}_{2y}^{[q]}(q+2)\frac{\partial^{q/2+1} f_2}{\partial y^{q/2+1}} + \mathcal{D}_{2y}^{[q]}(q+3)\frac{\partial^{q/2+1} f_4}{\partial y^{q/2+1}}.$$

Substitution of (14) and (15) into (12) yields

$$\left(\mathcal{D}_{2x}^{[q]}(1) f_1 + \mathcal{D}_{2x}^{[q]}(2) f_3 + \mathcal{D}_{2x}^{[q]}(3) f_5\right) + \left(\mathcal{D}_{2y}^{[q]}(1) f_2 + \mathcal{D}_{2y}^{[q]}(2) f_3 + \mathcal{D}_{2y}^{[q]}(3) f_4\right) = F_3 - R_{2x}^{[q]} - R_{2y}^{[q]}, \tag{16}$$

where $R_{2x}^{[q]}$ and $R_{2y}^{[q]}$ are known values taken from a previous iteration. It can be seen that the resultant algebraic systems have only 5 nonzero entries per row.

3.2 One dimensional IRBF approximations on the grid lines

To obtain nodal derivative values in $R_{2x}^{[q]}$ and $R_{2y}^{[q]}$ of (16), we also apply an IRBFq scheme on a grid line, where all nodes on the grid line are involved (Mai-Duy *et al.*, 2022). We use the notation $\bar{a}$ instead of a to denote the width/shape-parameter employed here. Let N_η be the number of nodes on a grid line. For the first biharmonic problem, the boundary values

of the first-order derivative of u are given. The presence of integration constants enables the derivative boundary values (i.e. $\partial u/\partial \eta$ at the two end-points of a grid line) to be included in the conversion system in an exact manner.

The kth-order derivative of u at η_i is expressed in terms of u at $(\eta_1, \eta_2, \ldots, \eta_{N_\eta})$ and its derivatives at (η_1, η_{N_η})

$$\frac{\partial^k u_i}{\partial \eta^k} = \widetilde{\mathcal{D}}_{k\eta}^{[q]} \widehat{u}, \tag{17}$$

where $\widetilde{\mathcal{D}}_{2\eta}^{[q]}$ is a row matrix of $(N_\eta+2)$ known coefficients and $\widehat{u} = \left(u_1, u_2, \ldots, u_{N_\eta}, \frac{\partial u_1}{\partial \eta}, \frac{\partial u_{N_\eta}}{\partial \eta}\right)^T$.

The kth-order derivative of v at η_i is expressed in terms of v at $(\eta_1, \eta_2, \ldots, \eta_{N_\eta})$

$$\frac{\partial^k v_i}{\partial \eta^k} = \overline{\mathcal{D}}_{k\eta}^{[q]} \widehat{v}, \tag{18}$$

where $\overline{\mathcal{D}}_{2\eta}^{[q]}$ is a row matrix of N_η known coefficients and $\widehat{v} = \left(v_1, v_2, \ldots, v_{N_\eta}\right)^T$.

3.3 Dirichlet boundary condition for an intermediate variable

The Dirichlet boundary condition for the variable v is computed through the discretised form of equation (4) on the boundary

$$v_b = \frac{\partial^2 u_b}{\partial x^2} + \frac{\partial^2 u_b}{\partial y^2}. \tag{19}$$

If the boundary is a straight line parallel to the x or y axis, equation (19) reduces, respectively, to

$$v_b = \frac{\partial^2 u_b}{\partial y^2} + p_x, \tag{20}$$

or

$$v_b = \frac{\partial^2 u_b}{\partial x^2} + p_y, \tag{21}$$

where p_x and p_y are some known values derived from the boundary values of u.

If the boundary is a curved line, one can establish the following analytical relationship

between $\partial^2 u_b/\partial x^2$ and $\partial^2 u_b/\partial y^2$ (Le-Cao *et al.*, 2009)

$$\frac{t_x}{t_y}\frac{\partial^2 u_b}{\partial x^2} - \frac{t_y}{t_x}\frac{\partial^2 u_b}{\partial y^2} = \frac{1}{t_y}\nabla_{\mathbf{t}}\left(\frac{\partial u_b}{\partial x}\right) - \frac{1}{t_x}\nabla_{\mathbf{t}}\left(\frac{\partial u_b}{\partial y}\right), \tag{22}$$

where t_x and t_y are the x and y components of a unit vector tangent to the boundary. Since u and $\partial u/\partial n$ are given along the boundary, the terms on RHS of (22) can be evaluated. Making use of (22), like (21) and (20), v_b in (19) can be expressed in terms of only $\partial^2 u_b/\partial x^2$ or only $\partial^2 u_b/\partial y^2$, which are used for computing v_b at the two end-nodes of a x grid line or a y grid line, respectively. We use (17) to compute $\partial^2 u_b/\partial \eta^2$ at a boundary node, where nodal values along the η grid line associated with that boundary node are used.

3.4 Solution procedure

The resulting algebraic systems can be solved by Picard iterations and Newton-like methods. They are iterative, where the solution is approached through a series of steps. The key difference between the two methods lies in the algorithm used within each step and how the current approximation is obtained from one or more previous approximations. Picard iterations are known as successive substitution, while Newton-like iterations are gradient-based methods. The former converges more slowly but involves less work per iteration than the latter (Dennis and Schnabel, 1996).

Newton-like methods: we apply the trust-region method (More and Sorensen, 1983), where the termination tolerance on the size of a step is set to 1.0×10^{-6}.

Picard iterations: the following solution procedure is implemented.

1. Set the nodal values of v and u and their derivatives, except for the boundary values of u and its first derivative, to zero.

2. Solve equation (4) for the variable u, subjected to the Dirichlet boundary condition (2).

3. Relax the solution u

$$\mathrm{sol}_u^k = \alpha \mathrm{sol}_u^k + (1-\alpha)\mathrm{sol}_u^{k-1}, \quad 0 < \alpha \leq 1,$$

where the superscript k is used to denote the current iteration and sol_u comprises the interior values of u

4. Compute derivatives of u along the grid lines, where the approximations are constructed to satisfy the boundary values of the first derivative of u.

5. Derive the boundary values for v, where equation (4) is reduced to the form that involves only the second derivative with respect to the coordinate of the associated grid line, and satisfies the boundary condition (3).

6. Compute the interior values of v using the data from Step 4 and regard it as the previous interior solution for v.

7. Solve equation (5) for the variable v, subjected to the Dirichlet boundary condition derived from Step 5.

8. Relax the solution v

$$\mathrm{sol}_v^k = \alpha \mathrm{sol}_v^k + (1-\alpha)\mathrm{sol}_v^{k-1}, \quad 0 < \alpha \leq 1,$$

where the superscript k is used to denote the current iteration and sol_v comprises the boundary and interior values of v.

9. Compute derivatives of v along the grid lines.

10. Check convergence

$$CM = \frac{\sqrt{\sum_i \left(u_i^k - u_i^{k-1}\right)^2 + \sum_i \left(v_i^k - v_i^{k-1}\right)^2}}{\sqrt{\sum_i \left(u_i^k\right)^2 + \sum_i \left(v_i^k\right)^2}},$$

where u_i^k and v_i^k are, respectively, the values of u and v from Step 2 and Step 7. If

CM is less than a specified tolerance, stop the calculation and output the results. Otherwise, repeat from Step 2. In this work, the tolerance is set to 1.0×10^{-10}.

The solving process typically takes a few hundred iterations when using the Picard method and only a relatively few iterations when using the trust-region method.

Since there are only 5 function values involved in the IRBF approximation of derivatives at an interior node, the proposed method results in sparse algebraic systems. Furthermore, it has the ability to handle the case of non-rectangular domains without using any coordinate transformations. On the other hand, one may need to use extended precision (32-digit accuracy) to handle local IRBF approximations (i.e. those on the stencils and those on the grid lines) and there is a need to compute derivatives along the grid lines. It is noted that (i) for local systems, the matrices are relatively small; (ii) on the grid lines, the approximations are simply problems of function approximation, where overlapping domain decomposition can be employed; (iii) one is still able to use double precision over grid lines of 200 nodes for the case of IRBF2; and (iv) the global system matrices are relatively large and they are constructed and solved in standard double precision (16-digit accuracy).

4 Numerical examples

The proposed IRBF method is implemented with the multiquadric function.

4.1 Example 1

The method is first tested with the first biharmonic equation defined in the square $-1 \leq x, y \leq 1$. The forcing function and exact solution to this problem are

$$b(x,y) = 4\sin(\pi x)\sin(\pi y), \tag{23}$$

$$u(x,y) = \frac{1}{\pi^4}\sin(\pi x)\sin(\pi y). \tag{24}$$

The boundary conditions u and $\partial u/\partial n$ are derived from (24). We employ IRBFq with $q = (2, 4, 6, 8)$ to construct the approximations on the stencil and grid lines.

Approximations on the stencil: These approximations affect the accuracy of the solution, N_e, and the condition number of the system matrix, $cond(\mathcal{A})$. Another quantity of interest is the condition number of the conversion matrix, $cond(\mathcal{C})$. Figures 2, 3 and 4 show the effect of the RBF width a on N_e, $cond(\mathcal{C})$ and $cond(\mathcal{A})$, respectively. For the approximations along the grid lines, the RBF width is chosen as $\bar{a} = 0.01$. With regard to the solution accuracy, it can be seen that the IRBF solution is much more accurate and much less dependent on the RBF width with an increase in the order of the IRBF scheme. It appears that the IRBF2 solution does not converge with grid refinement for relatively-large values of a. For the case of using IRBF6 and IRBF8, the IRBF solution is highly accurate over a wide range of the RBF width. There is no need for searching the optimal RBF width. For $a = 10^{-5}$ and $a = 10^{-2}$, the solution converges, respectively, as $O(h^{3.69})$ and $O(h^{2.29})$ for IRBF4, $O(h^{7.00})$ and $O(h^{7.30})$ for IRBF6, and $O(h^{9.09})$ and $O(h^{9.08})$ for IRBF8. With regard to the conversion matrix $\mathcal{C}$, the condition number does not grow much with the RBF width, especially for coarse grids. The use of an IRBF scheme of higher order and/or a grid of higher density produces a larger condition number. With regard to the system matrix $\mathcal{A}$, it can be seen that the condition number is relatively small and not influenced by the RBF width.

Approximations on the grid lines: These approximations affect the accuracy of the solution, N_e, but not affect the condition number of the system matrix, $cond(\mathcal{A})$. Other important quantities are the condition numbers of the conversion matrix for u, $cond(\mathcal{C}_u)$, and for v, $cond(\mathcal{C}_v)$. For the approximations on the stencils, the RBF width is taken as $a = 0.001$. Figures 5, 6 and 7 show the effect of the RBF width a on N_e, $cond(\mathcal{C}_u)$ and $cond(\mathcal{C}_v)$, respectively. With regard to the solution accuracy, it can be seen that the IRBF solution is more accurate and less dependent on the RBF width with an increase in the order of the IRBF scheme. It appears that the IRBF2 solution is unstable with grid refinement. For $\bar{a} = 10^{-5}$ and $\bar{a} = 10^{-2}$, the solution converges, respectively, as $O(h^{4.09})$ and $O(h^{3.58})$ for IRBF4, $O(h^{6.87})$ and $O(h^{7.01})$ for IRBF6, $O(h^{9.05})$ and $O(h^{9.09})$ for IRBF8. With regard to

the conversion matrices, it can be seen that the condition numbers are not influenced much by the RBF width. A higher-order IRBF scheme and a higher-density grid produce a larger condition number.

4.2 Example 2

Consider the first biharmonic equation with the forcing function

$$b = (2\pi)^4 \left[4\cos(2\pi x)\cos(2\pi y) - \cos(2\pi x) - \cos(2\pi y)\right], \tag{25}$$

and the domain being a region inside the unit square and outside the circle of radius 0.125 (Figure 8). The exact solution is given by

$$u = \left[1 - \cos(2\pi x)\right]\left[1 - \cos(2\pi y)\right], \tag{26}$$

from which the boundary conditions u and $\partial u/\partial n$ are derived. We also use a Cartesian grid to represent the domain. The boundary nodes are intersections of the grid lines and the boundaries. In generating the interior nodes, the grid nodes close to the inner boundary (within distance $h/6$, where h is the grid size) are removed (Figure 8). We employ IRBFq with $q = (2, 4, 6, 8)$ to construct the approximations on the stencil and grid lines.

Approximations on the stencil: Results concerning the accuracy of the solution, N_e, against the RBF width on the stencils, a, are shown in Figure 9, where the RBF width $\bar{a}$ for the approximations on the grid lines is kept at value of 0.01. The influence of the RBF width (stencils) becomes less with an increase in the order of the IRBF scheme. It appears that the IRBF2 solution does not converge with grid refinement for large values of a. For the case of using IRBF6 and IRBF8, the IRBF solution is highly accurate over a wide range of the RBF width. There is no need for searching the optimal RBF width. For $a = 10^{-5}$ and $a = 10^{-2}$, the solution converges, respectively, as $O(h^{3.53})$ and $O(h^{2.10})$ for IRBF4, $O(h^{8.51})$ and $O(h^{8.43})$ for IRBF6, and $O(h^{11.34})$ and $O(h^{11.35})$ for IRBF8.

Approximations on the grid lines: Results concerning the accuracy of the solution, N_e, against the RBF width on the grid lines, $\bar{a}$, are shown in Figure 10, where the RBF width a for the approximations on the stencils is kept at value of 0.001. The influence of the RBF width (grid lines) becomes less with an increase in the order of the IRBF scheme. It can be seen that the IRBF2 solution is unstable with respect to grid refinement. For the case of using IRBF6 and IRBF8, the IRBF solution is highly accurate over a wide range of the RBF width. There is no need for searching the optimal RBF width. For $\bar{a} = 10^{-5}$ and $\bar{a} = 10^{-2}$, the solution converges, respectively, as $O(h^{4.35})$ and $O(h^{3.40})$ for IRBF4, $O(h^{8.36})$ and $O(h^{8.51})$ for IRBF6, and $O(h^{11.26})$ and $O(h^{11.34})$ for IRBF8.

4.3 Example 3

Consider the steady viscous flow in a square cavity with the side length L driven by a lid that translates parallel to itself with a velocity U. The boundary conditions for the stream function are

$$\psi = 0 \qquad \text{over all walls,} \tag{27}$$

$$\frac{\partial \psi}{\partial x} = 0 \qquad \text{at the sides,} \tag{28}$$

$$\frac{\partial \psi}{\partial y} = 0 \qquad \text{at the bottom,} \tag{29}$$

$$\frac{\partial \psi}{\partial y} = U \qquad \text{at the lid.} \tag{30}$$

The Reynolds number is defined as $Re = UL/\nu$, where ν is the kinematic viscosity of the fluid. This is a well-known benchmark problem for the assessment of numerical methods and the validation of computer codes (Botella and Peyret, 1998).

We simulate the lid-driven cavity flow at the Reynolds number of 0, 100, 400, 1000, 3200, 5000, 7500 and 10000. A trust-region method is used to solve the resulting nonlinear system of algebraic equations. It is noted that the Picard iteration scheme is appropriate for only $Re \leq 5000$. We take a computed solution at a lower adjacent Re as the initial solution.

In computing the derivatives of ω along the grid lines, the boundary values of the first derivative of ω (i.e. $\partial^3\psi_b/\partial x^3$ on the x grid lines and $\partial^3\psi_b/\partial y^3$ on the y grid lines) are included in the conversion matrices to enhance the approximation quality. The IRBF8 results are compared with the benchmark finite-difference solutions (Ghia *et al.*, 1982) and the benchmark spectral results (Botella and Peyret, 1998). The latter was mainly reported for $Re = 1000$. By reference to the spectral results (converged to 7 digits for the velocities), Table 1 shows that the percentage of the relative error is small and reduced with an increase in the grid density. The errors found from a grid of 121×121 are lower than 0.05% while they are up to 2% for the finite-difference results found from a grid of 129×129 in (Ghia *et al.*, 1982). Figures 11 and 12 display, respectively, the streamlines and iso-vorticity lines of the flow at high $Re = (3200, 5000, 7500, 10000)$ using a uniform grid of 161×161. They all look reasonable. The IRBF solution for $Re = 10000$ using only $161 \times 161 = 25921$ nodes are competitive with those found in the literature using 66049 nodes (Ghia *et al.*, 1982) and 39389 nodes (Bayona *et al.*, 2017).

4.4 Example 4

We numerically study the steady viscous flow in an equilateral triangular cavity with one moving wall. This problem is also considered as an important test case for numerical techniques. The three corners of the cavity are chosen as $(0, 0)$, $(\sqrt{3}, 3)$ and $(-\sqrt{3}, 3)$. The boundary conditions are that the velocity is constant U along the top and zero on fixed walls. Unlike the rectangle, the triangle cannot be mapped onto a square without a singularity (Karunasena *et al.*, 1996). The flow has been simulated by means of finite differences. In (McQuain *et al.*, 1994), the stream function formulation was employed. It was found that the finite-difference stencils for the fourth-order PDEs as used for the trapezoid and rectangle fail completely for the triangle. As a result, the equilateral triangle was mapped to an isosceles right triangle and nonsymmetric finite-differences stencils were developed to yield well-conditioned algebraic systems that are solved by using a Newton-like iteration. The finite-difference results were reported for Re up to 500. In (Li and Tang, 1996), the

stream function and vorticity formulation was employed. The PDEs were also solved on a transformed geometry and the results were reported for Re up to 1500. The flow in a triangular cavity has also been simulated by other types of numerical techniques such as the finite-element method (Kohno and Bathe, 2006) and the control volume method (Jyotsna and Vanka, 1995).

In this work, the PDEs are solved on the original geometry (no coordinate transformations implemented). We simply use a Cartesian grid to represent the triangle (Figure 13). For any Cartesian grid used, the grid lines near the corners involves only 3 grid nodes, and the use of low-order IRBF schemes to compute the derivatives along these grid lines appears more appropriate. In discretisation, we employ IRBF2 on all the grid lines and IRBF8 on the stencils. Like (McQuain *et al.*, 1994), we also choose the reference length and velocity as $L = 1$ and $U = 1$, respectively. Values of Re, namely 0, 100, 200, 500, 1000, 1500 and 2000, are considered. We solve the algebraic systems resulting from the IRBF discretisation using the trust-region method. The IRBF results were reported in Figure 14 for the streamline patterns and in Figure 15 for the vorticity distribution. They all look reasonable. Table 2 displays the calculated centre locations of the primary vortex and the corresponding stream function ψ_c and vorticity ω_c. Results from the finite-difference schemes (McQuain *et al.*, 1994; Li and Tang, 1996) are also included for comparison purposes. It can be seen that the present results are in good agreement with the finite-difference results for the cases $Re = 100$ and 200, and become somehow different when $Re \geq 500$. We further check our results through plotting the location of the centre of the primary eddy as a function of the Reynolds number. As shown in Figure 16, the location changes smoothly with an increase in Re; our results are in better agreement with those by the flow-condition-based interpolation finite-element method (Kohno and Bathe, 2006).

5 Concluding remarks

This paper reports an effective high-order discretisation method, based on compact local integrated-RBF approximations and Cartesian grids, for solving the first biharmonic equation in a coupled set of two Poisson equations. The proposed method results in algebraic systems that have only 5 nonzero entries per row. Unlike central-difference schemes, the method is able to yield a fast rate of convergence with grid refinement (up to about 11) and can handle the case of non-rectangular domains without using coordinate transformations. Unlike traditional RBF methods, the present RBF solutions are not sensitive to the change of the RBF width. The method is tested successfully in several flows that are of primary importance in practice, including the flow in a triangular cavity.

References

1. Abbaszadeh, M., Pourbashash, H. and Khaksar-e Oshagh, M. (2022), "The local meshless collocation method for solving 2D fractional Klein-Kramers dynamics equation on irregular domains", *International Journal of Numerical Methods for Heat & Fluid Flow*, Vol. 32 No. 1, pp. 41-61.

2. Bayona, V., Flyer, N., Fornberg, B. and Barnett, G.A. (2017), "On the role of polynomials in RBF-FD approximations: II. Numerical solution of elliptic PDEs", *Journal of Computational Physics*, Vol. 332, pp. 257-273.

3. Botella, O. and Peyret, R. (1998), "Benchmark spectral results on the lid-driven cavity flow", *Computers & Fluids*, Vol. 27 No. 4, pp. 421-433.

4. Collatz, L. (1960), *The Numerical Treatment of Differential Equations*, Springer–Verlag, Berlin.

5. Dehghan, M. and Mohebbi, A. (2006), "Multigrid solution of high order discretisation for three-dimensional biharmonic equation with Dirichlet boundary conditions of second kind", *Applied Mathematics and Computation*, Vol. 180 No. 2, pp. 575-593.

6. Dehghan, M. and Shokri, A. (2008), "A numerical method for solution of the two-dimensional sine-Gordon equation using the radial basis functions", *Mathematics and Computers in Simulation*, Vol. 79 No. 3, pp. 700-715.

7. Dennis, J.E. and R.B. Schnabel. (1996), *Numerical Methods for Unconstrained Optimization and Nonlinear Equations*, Society for Industrial and Applied Mathematics, Philadelphia.

8. Ebrahimijahan, A., Dehghan, M. and Abbaszadeh, M. (2020), "Compact local integrated radial basis functions (Integrated RBF) method for solving system of non–linear advection-diffusion-reaction equations to prevent the groundwater contamination", *Engineering Analysis with Boundary Elements*, Vol 121, pp. 50-64.

9. Ebrahimijahan, A. and Dehghan, M. (2021), "The numerical solution of nonlinear generalized Benjamin–Bona–Mahony–Burgers and regularized long-wave equations via the meshless method of integrated radial basis functions", *Engineering with Computers*, Vol. 37, pp. 93–122.

10. Ebrahimijahan, A., Dehghan, M. and Abbaszadeh, M. (2022), "Simulation of Maxwell equation based on an ADI approach and integrated radial basis function-generalized moving least squares (IRBF-GMLS) method with reduced order algorithm based on proper orthogonal decomposition", *Engineering Analysis with Boundary Elements*, Vol 143, pp. 397-417.

11. Ebrahimijahan, A., Dehghan, M. and Abbaszadeh, M. (2022b), "Integrated radial basis functions (IRBFs) to simulate nonlinear advection–diffusion equations with smooth and non-smooth initial data", *Engineering with Computers*, Vol. 38, pp. 1071–1106.

12. Ghia, U., Ghia, K.N. and Shin, C.T. (1982), "High-Re solutions for incompressible flow using the Navier-Stokes equations and a multigrid method", *Journal of Computational Physics*, Vol. 48 No. 3, pp. 387-411.

13. Gupta, M.M. and Manohar R.P. (1979), "Direct solution of the biharmonic equation using noncoupled approach", *Journal of Computational Physics*, Vol. 33 No. 2, pp.

236-248.

14. Hirsh, R.S. (1975), "Higher order accurate difference solutions of fluid mechanics problems by a compact differencing technique", *Journal of Computational Physics*, Vol. 19 No. 1, pp. 90–109.

15. Jyotsna, R. and Vanka, S.P. (1995), "Multigrid Calculation of Steady, Viscous Flow in a Triangular Cavity", *Journal of Computational Physics*, Vol. 122 No. 1, pp. 107-117.

16. Karunasena, W., Kitipornchai, S. and Al-Bermani, F.G.A. (1996), "Free vibration of cantilevered arbitrary triangular Mindlin plates", *International Journal of Mechanical Sciences*, Vol. 38 No. 4, pp. 431-442.

17. Kohno, H. and Bathe, K.-J. (2006), "A flow-condition-based interpolation finite element procedure for triangular grids", *International Journal for Numerical Methods in Fluids*, Vol. 51, pp. 673-699.

18. Kosec, G. and Šarler, B. (2008), "Solution of thermo-fluid problems by collocation with local pressure correction", *International Journal of Numerical Methods for Heat & Fluid Flow*, Vol. 18 No. 7/8, pp. 868-882

19. Kosec, G. and Šarler, B. (2013), "Solution of a low Prandtl number natural convection benchmark by a local meshless method", *International Journal of Numerical Methods for Heat & Fluid Flow*, Vol. 23 No. 1, pp. 189-204.

20. Le-Cao, K., Mai-Duy, N. and Tran-Cong, T. (2009), "An effective integrated-RBFN cartesian-grid discretization for the stream function–vorticity–temperature formulation in nonrectangular domains", *Numerical Heat Transfer, Part B: Fundamentals*, Vol. 55 No. 6, pp. 480-502.

21. Li, M. and Tang, T. (1996), "Steady viscous flow in a triangular cavity by efficient numerical techniques", *Computers & Mathematics with Applications*, Vol. 31 No. 10, pp. 55-65.

22. Mai-Duy, N. and Tanner, R.I. (2005), "Computing non-Newtonian fluid flow with radial basis function networks", *International Journal for Numerical Methods in Fluids*, Vol. 48, pp. 1309-1336.

23. Mai-Duy, N. and Tanner, R.I. (2007),"A collocation method based on one-dimensional RBF interpolation scheme for solving PDEs", *International Journal of Numerical Methods for Heat & Fluid Flow*, Vol. 17 No. 2, pp. 165-186.

24. Mai-Duy, N. and Strunin, D. (2021), "New approximations for one-dimensional 3-point and two-dimensional 5-point compact integrated RBF stencils", *Engineering Analysis with Boundary Elements*, Vol. 125, pp. 12-22.

25. Mai-Duy, N., Strunin, D. and Karunasena, W. (2022), "Computing high-order derivatives in compact integrated-RBF stencils", *Engineering Analysis with Boundary Elements*, Vol. 135, pp. 369-381.

26. Mai-Duy, N., Strunin, D. and Karunasena, W. (2022b), "A new high-order nine-point stencil, based on integrated-RBF approximations, for the first biharmonic equation", *Engineering Analysis with Boundary Elements*, Vol. 143, pp. 687-699.

27. McQuain, W.D., Ribbens, C.J., Wang, C.-Y. and Watson, L.T. (1994), "Steady viscous flow in a trapezoidal cavity", *Computers & Fluids*, Vol. 23 No. 4, pp. 613-626.

28. Mesgarani, H., Kermani, M. and Abbaszadeh, M. (2022), "Application of SPD-RBF method of lines for solving nonlinear advection–diffusion–reaction equation with variable coefficients", *International Journal of Numerical Methods for Heat & Fluid Flow*, Vol. 32 No. 2, pp. 850-886.

29. Mohebbi, A., Abbaszadeh, M. and Dehghan, M. (2014), "The meshless method of radial basis functions for the numerical solution of time fractional telegraph equation", *International Journal of Numerical Methods for Heat & Fluid Flow*, Vol. 24 No. 8, pp. 1636-1659.

30. More, J.J. and Sorensen, D.C. (1983), "Computing a trust region step", *SIAM Journal on Scientific and Statistical Computing*, Vol. 4 No. 3, pp. 553-572.

31. Ngo-Cong, D., Tien, C.M.T., Nguyen-Ky, T., An-Vo, D.-A., Mai-Duy, N., Strunin, D.V. and Tran-Cong, T. (2017), "A generalised finite difference scheme based on compact integrated radial basis function for flow in heterogeneous soils", *International Journal for Numerical Methods in Fluids*, Vol. 85, pp. 404– 429.

32. Roache P.J. (1998), *Fundamentals of Computational Fluid Dynamics*, Hermosa Publishers, Albuquerque.

33. Stephenson, J.W. (1984), "Single cell discretizations of order two and four for biharmonic problems", *Journal of Computational Physics*, Vol. 55 No 1, pp. 65-80.

Table 1: Lid-driven square-cavity flow: Velocity extremes on the centerlines at $Re = 1000$. The percentage error is measured relative to the benchmark special results (Botella and Peyret, 1998). The errors found from a grid of 101×101 are lower than 0.05% while they are up to 2% for the finite-difference results found from a grid of 129×129 in (Ghia *et al.*, 1982).

Grid	y_{min}	$(v_x)_{min}$	Error(%)	x_{max}	$(v_y)_{max}$	Error(%)	x_{min}	$(v_y)_{min}$	Error(%)
81×81	0.1720	-0.3884	0.03	0.1580	0.3767	0.06	0.9090	-0.5270	0.01
101×101	0.1720	-0.3885	0.02	0.1580	0.3768	0.03	0.9090	-0.5270	0.01
121×121	0.1720	-0.3885	0.01	0.1580	0.3769	0.02	0.9090	-0.5270	0.01
141×141	0.1720	-0.3885	0.01	0.1580	0.3769	0.01	0.9090	-0.5271	0.01

Table 2: Lid-driven triangular-cavity flow: the location of the centre of the primary eddy and the corresponding stream function and vorticity for a grid of 12206 nodes.

Re	Method	$x_c + \sqrt{3}$	y_c	$\lvert\psi_c\rvert$	ω_c
100	Proposed	2.0667	2.3574	0.2481	1.3641
	Finite differences (McQuain *et al.*, 1994)	2.061	2.355	0.247	1.373
	Finite differences (Li and Tang, 1996)	2.100	2.363	0.244	1.264
200	Proposed	1.9349	2.2750	0.2621	1.2489
	Finite differences (McQuain *et al.*, 1994)	1.940	2.280	0.260	1.272
	Finite differences (Li and Tang, 1996)	1.905	2.250	0.262	1.156
500	Proposed	1.8657	2.2183	0.2765	1.1727
	Finite differences (McQuain *et al.*, 1994)	1.905	2.265	0.269	1.250
	Finite differences (Li and Tang, 1996)	1.840	2.213	0.278	1.124
1000	Proposed	1.8425	2.1956	0.2825	1.1509
	Finite differences (Li and Tang, 1996)	1.840	2.138	0.279	1.048
1500	Proposed	1.8351	2.1890	0.2847	1.1464
	Finite differences (Li and Tang, 1996)	1.840	2.138	0.277	0.998
2000	Proposed	1.8335	2.1881	0.2855	1.1477

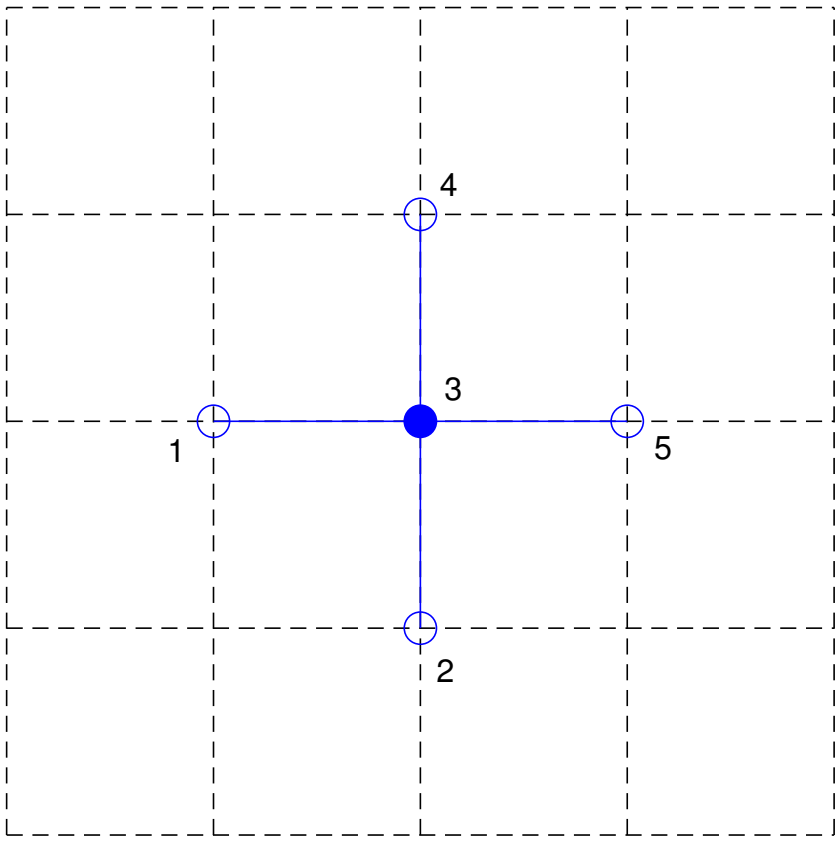

Figure 1: A five-point stencil.

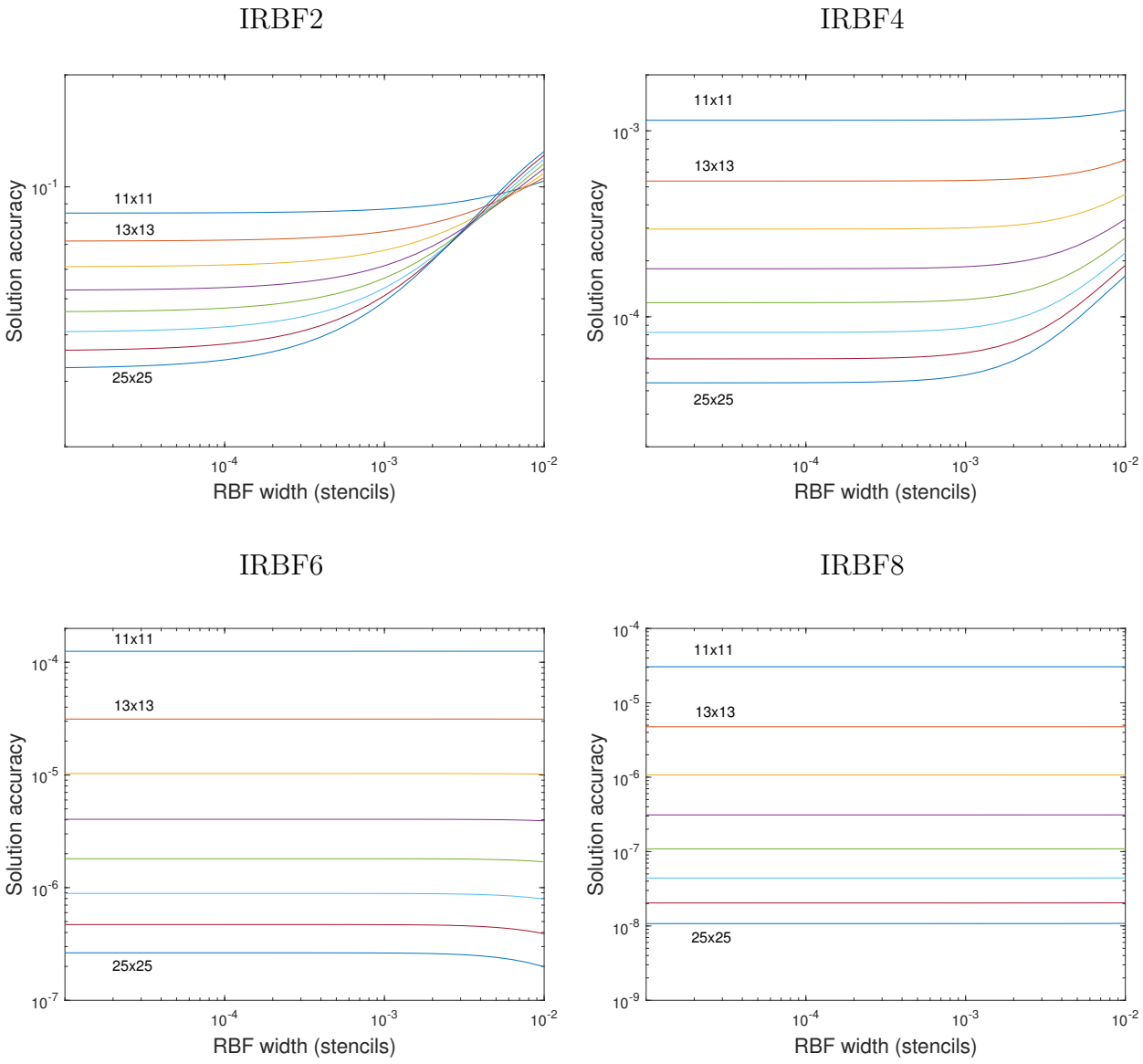

Figure 2: Example 1, $N_x \times N_y = (11 \times 11, 13 \times 13, \ldots, 25 \times 25)$: the solution accuracy, N_e, against the RBF width on the stencils, a. It appears that the IRBF2 solution does not converge with grid refinement for large values of a. For $a = 10^{-5}$ and $a = 10^{-2}$, the solution converges, respectively, as $O(h^{3.69})$ and $O(h^{2.29})$ for IRBF4, $O(h^{7.00})$ and $O(h^{7.30})$ for IRBF6, and $O(h^{9.09})$ and $O(h^{9.08})$ for IRBF8. It can be seen that the IRBF solution is more accurate and less dependent on the RBF width with an increase in the order of the IRBF scheme.

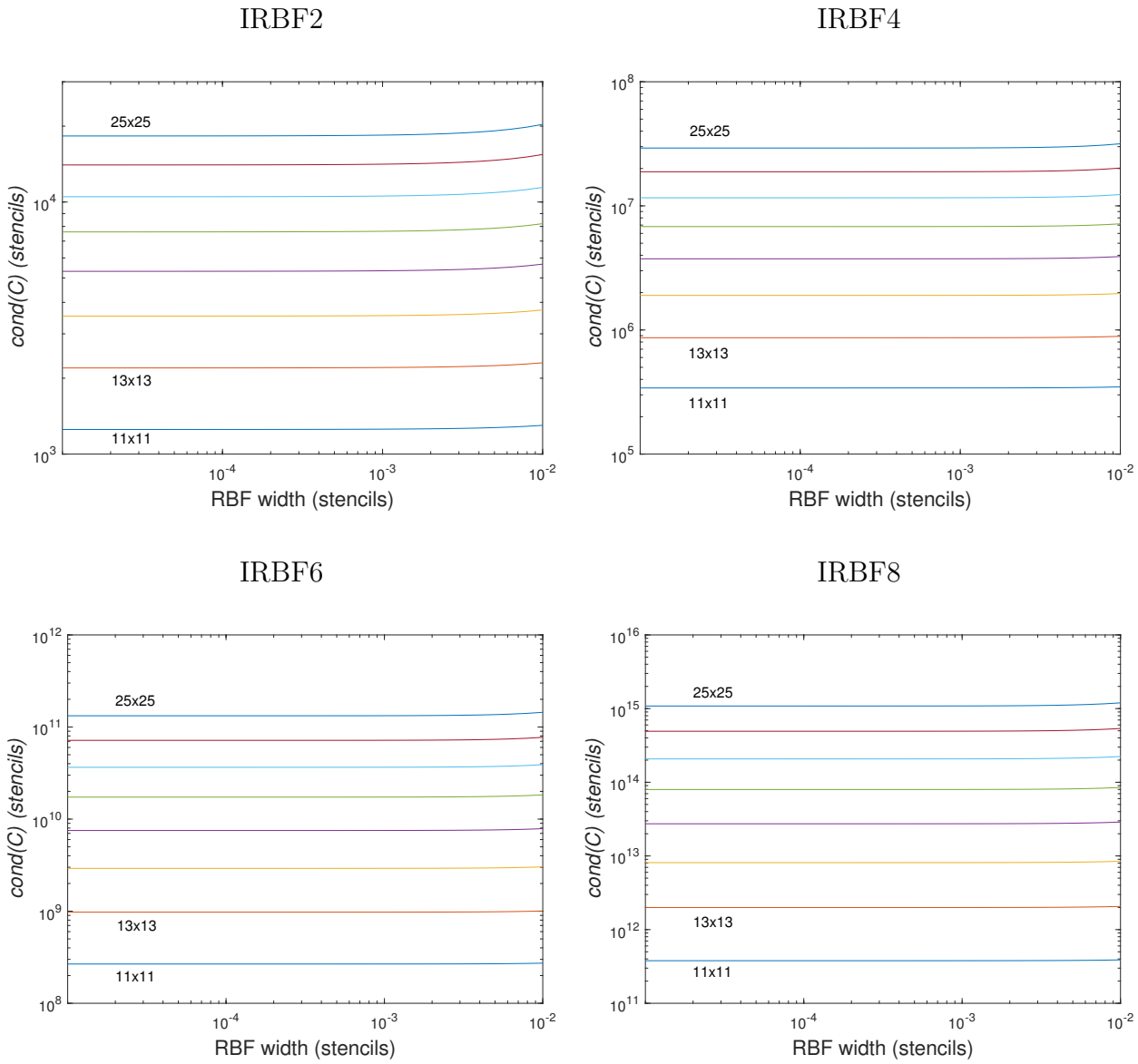

Figure 3: Example 1, $N_x \times N_y = (11 \times 11, 13 \times 13, \ldots, 25 \times 25)$: the condition number of the conversion matrix on the stencil, $cond(C)$, against the RBF width on the stencils, a. The condition number is not influenced much by the RBF width. A higher-order IRBF scheme and a higher-density grid produce a larger condition number.

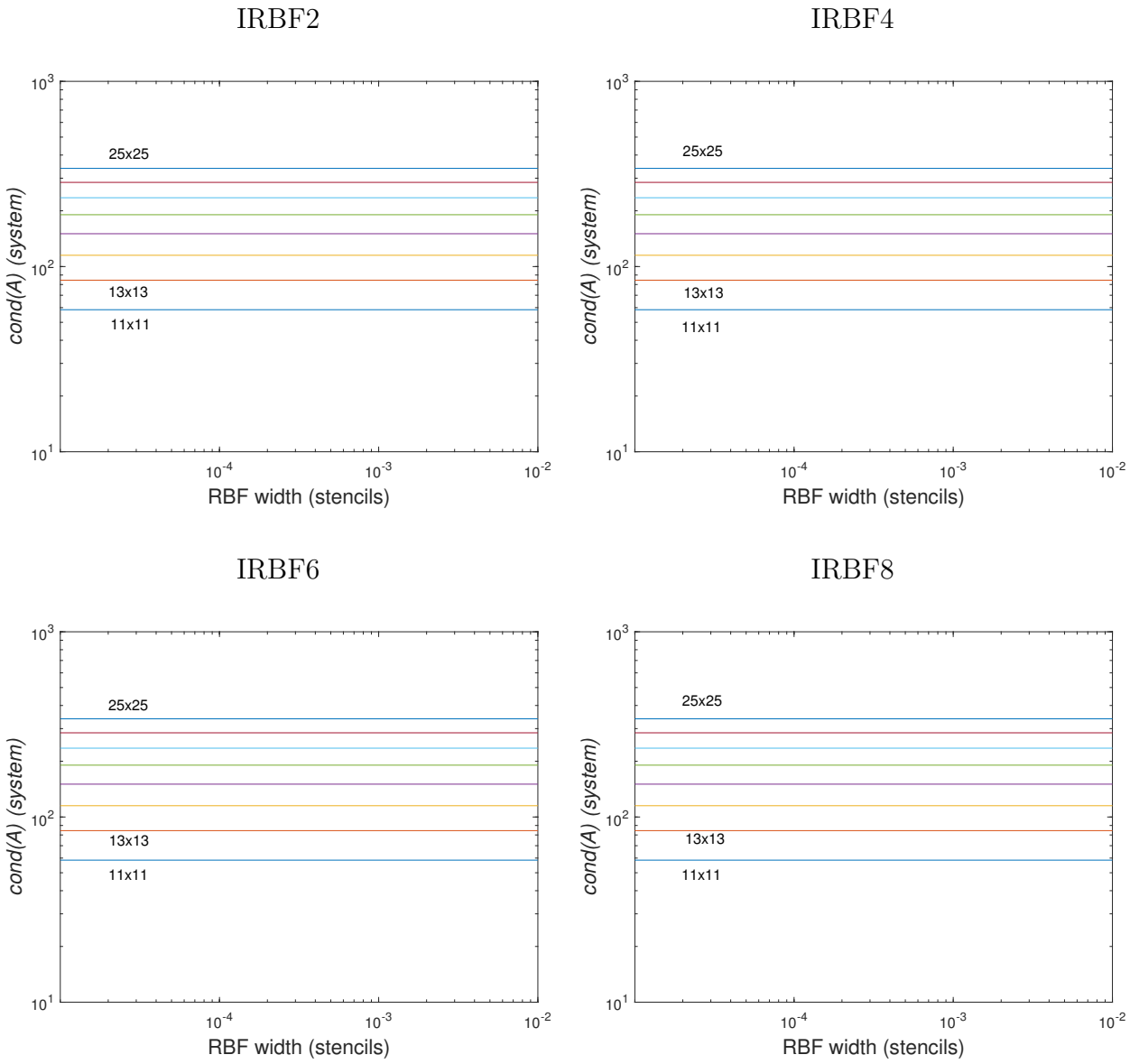

Figure 4: Example 1, $N_x \times N_y = (11 \times 11, 13 \times 13, \ldots, 25 \times 25)$: the condition number of the system matrix, $cond(A)$, against the RBF width on the stencils, a. The condition number is relatively small and not influenced much by the RBF width.

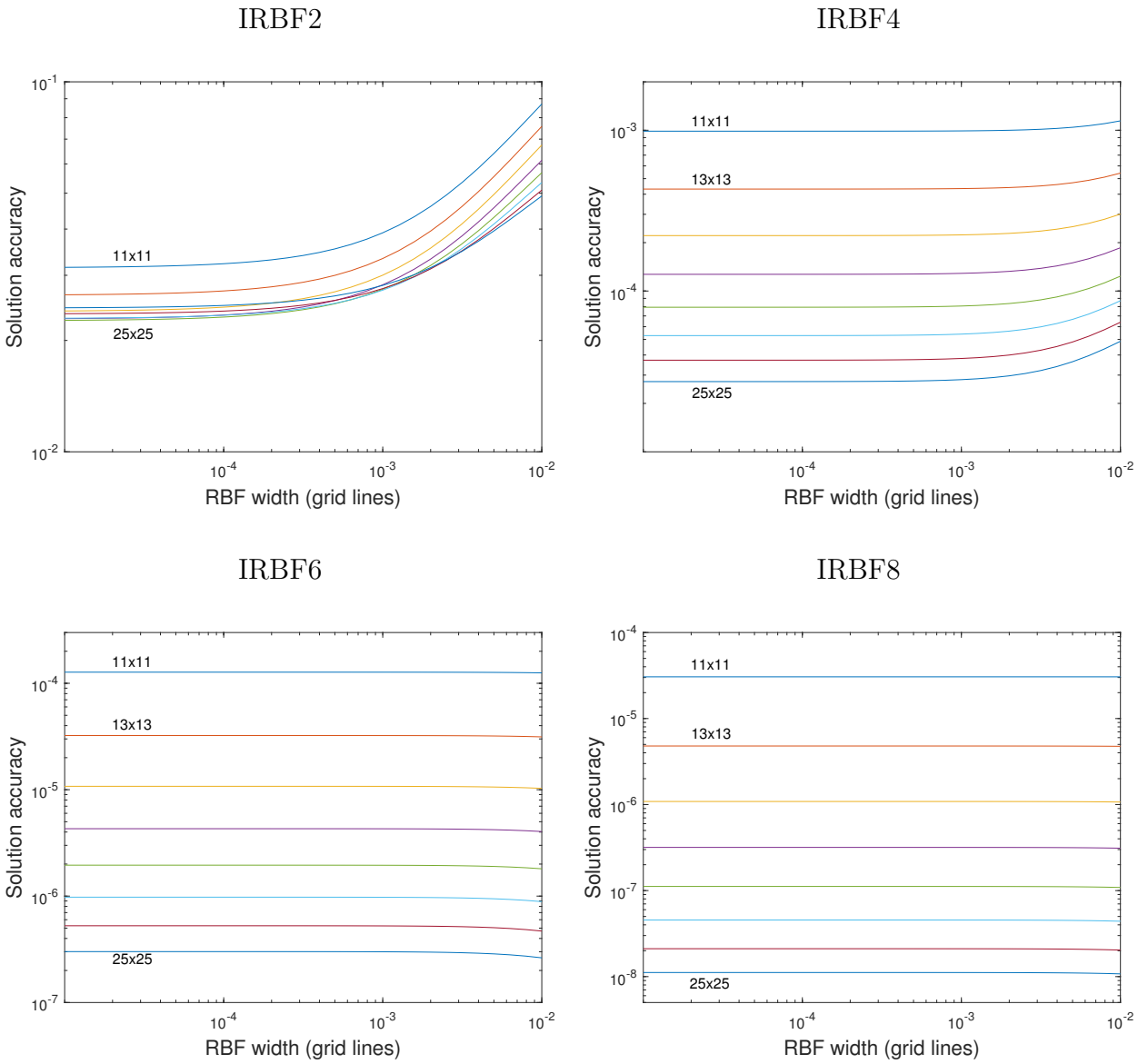

Figure 5: Example 1, $N_x \times N_y = (11 \times 11, 13 \times 13, \ldots, 25 \times 25)$: the solution accuracy, N_e, against the RBF width on the grid lines, $\bar{a}$. It appears that the IRBF2 solution is unstable with grid refinement. For $\bar{a} = 10^{-5}$ and $\bar{a} = 10^{-2}$, the solution converges, respectively, as $O(h^{4.09})$ and $O(h^{3.58})$ for IRBF4, $O(h^{6.87})$ and $O(h^{7.01})$ for IRBF6, and $O(h^{9.05})$ and $O(h^{9.09})$ for IRBF8. It can be seen that the IRBF solution is more accurate and less dependent on the RBF width with an increase in the order of the IRBF scheme.

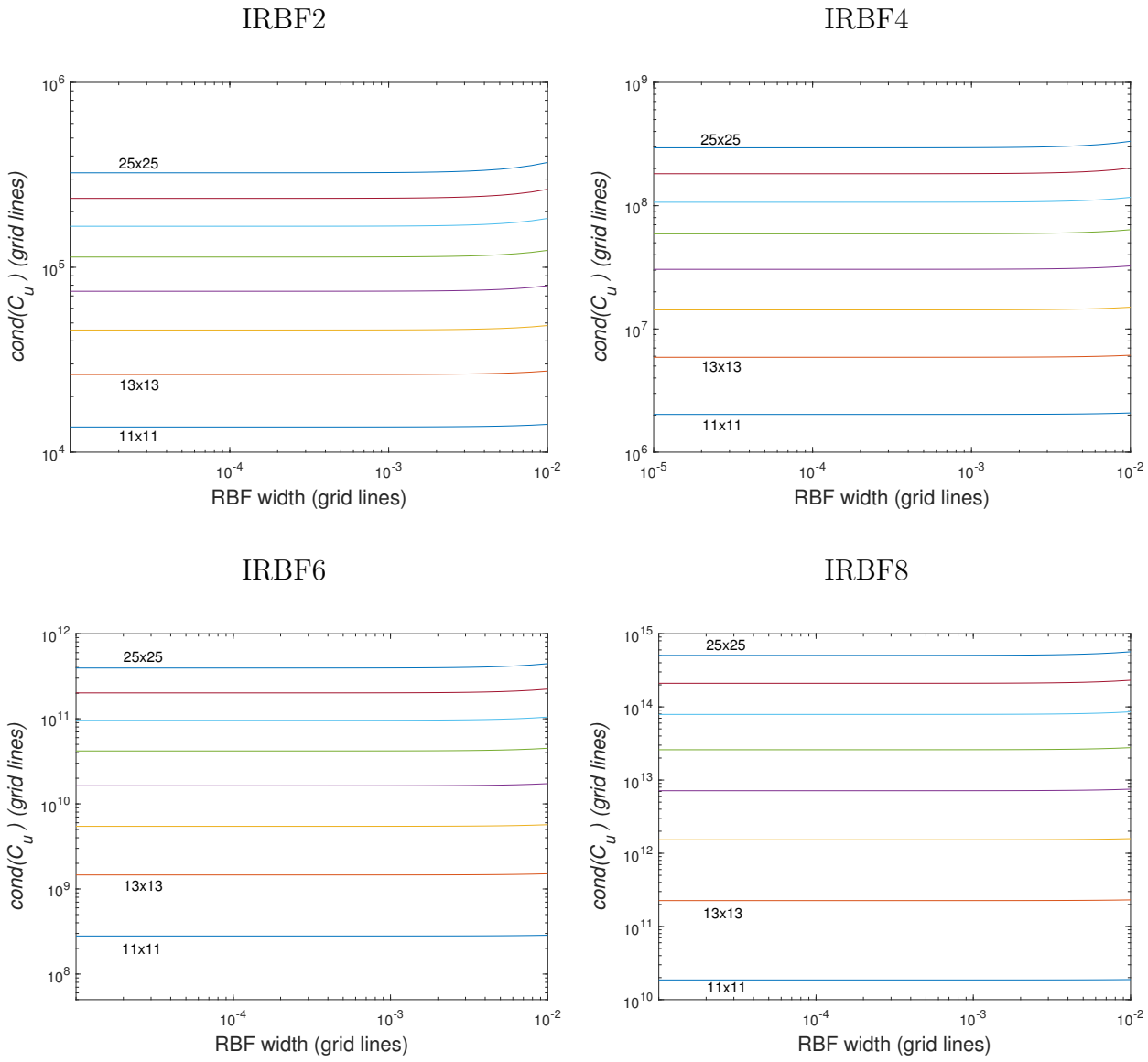

Figure 6: Example 1, $N_x \times N_y = (11 \times 11, 13 \times 13, \ldots, 25 \times 25)$: the matrix condition number, $cond(\mathcal{C})_u$, against the RBF width, $\bar{a}$, on the grid lines. The condition number is not influenced much by the RBF width. A higher-order IRBF scheme and a higher-density grid produce a larger condition number.

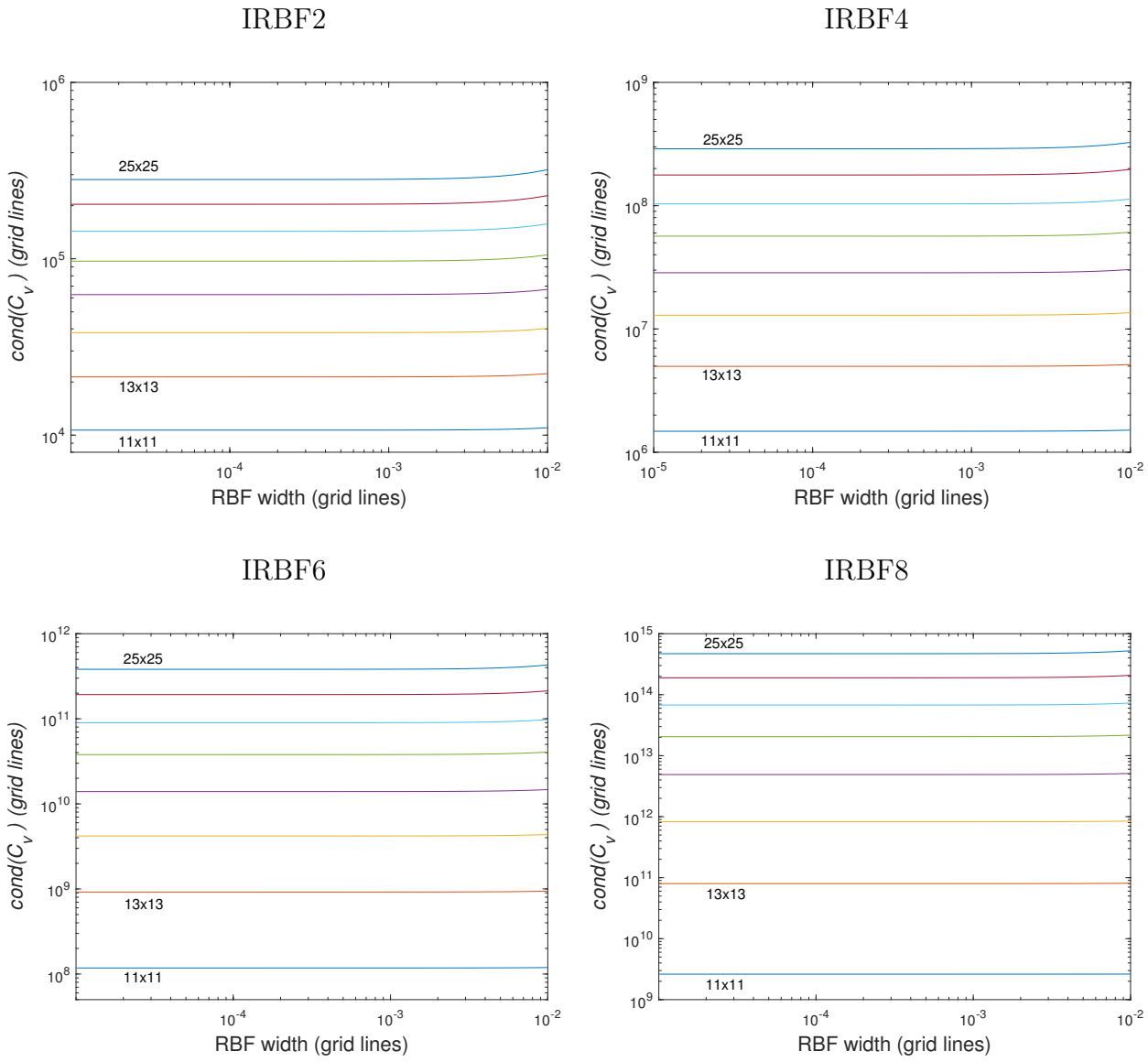

Figure 7: Example 1, $N_x \times N_y = (11 \times 11, 13 \times 13, \ldots, 25 \times 25)$: the matrix condition number, $cond(\mathcal{C})_v$, against the RBF width, $\bar{a}$, on the grid lines. The condition number is not influenced much by the RBF width. A higher-order IRBF scheme and a higher-density grid produce a larger condition number.

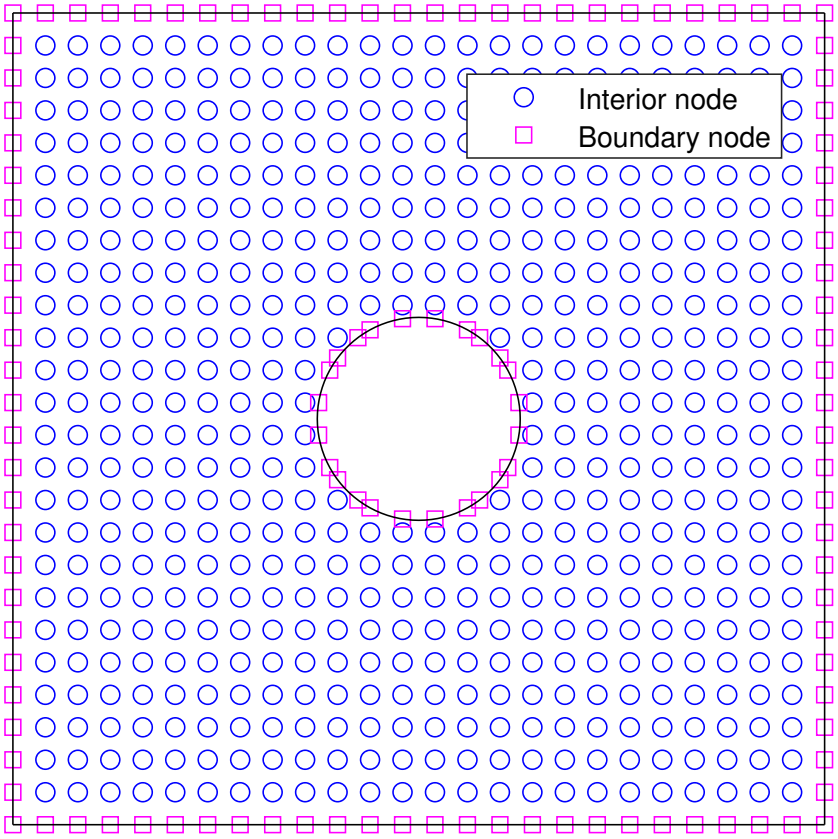

Figure 8: A non-simply connected domain and its associated discretisation.

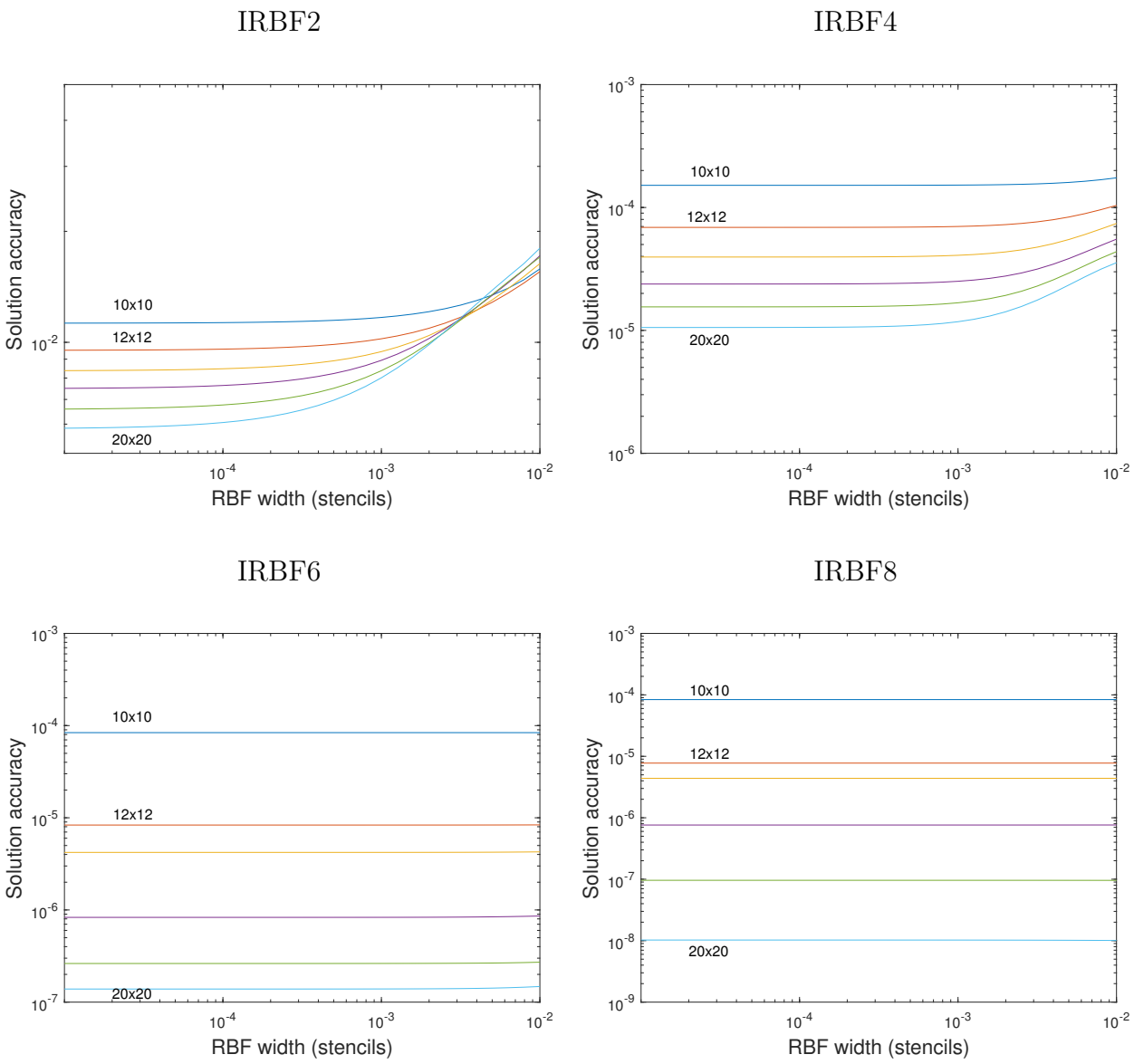

Figure 9: Non-rectangular domain, $N_x \times N_y = (10 \times 10, 12 \times 12, \ldots, 20 \times 20)$: the solution accuracy, N_e, against the RBF width on the stencils, a. For the approximations on the grid lines, the RBF width $\bar{a}$ is kept at value of 0.01. The influence of the RBF width (stencils) becomes less with an increase in the order of the IRBF scheme. It appears that the IRBF2 solution does not converge with grid refinement for large values of a. For $a = 10^{-5}$ and $a = 10^{-2}$, the solution converges, respectively, as $O(h^{3.53})$ and $O(h^{2.10})$ for IRBF4, $O(h^{8.51})$ and $O(h^{8.43})$ for IRBF6, and $O(h^{11.34})$ and $O(h^{11.35})$ for IRBF8.

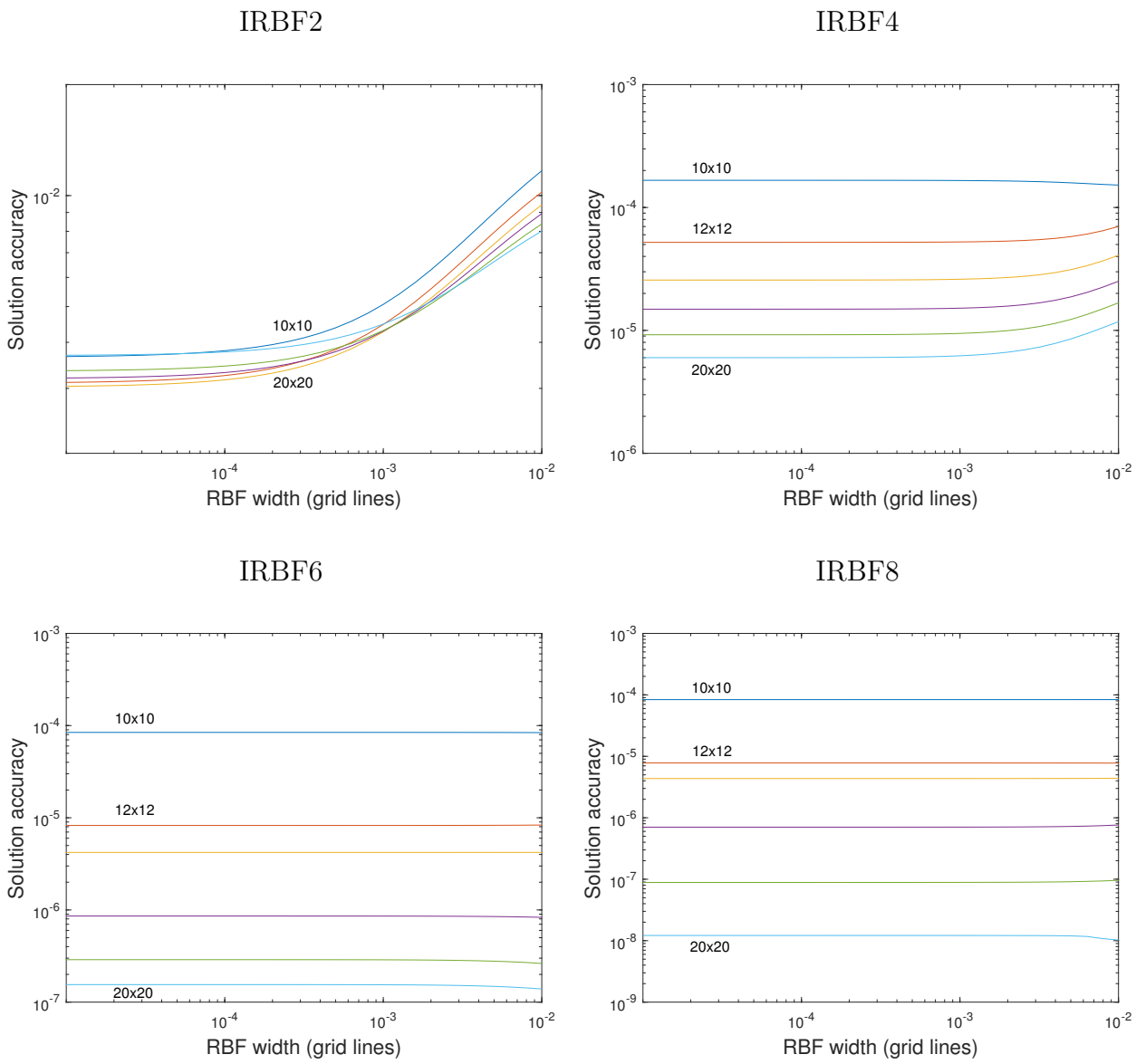

Figure 10: Non-rectangular domain, $N_x \times N_y = (10 \times 10, 12 \times 12, \ldots, 20 \times 20)$: the solution accuracy, N_e, against the RBF width on the grid lines, $\bar{a}$. For the approximations on the stencils, the RBF width a is kept at value of 0.001. The influence of the RBF width (grid lines) becomes less with an increase in the order of the IRBF scheme. It can be seen that the IRBF2 solution is unstable with respect to grid refinement. For $\bar{a} = 10^{-5}$ and $\bar{a} = 10^{-2}$, the solution converges, respectively, as $O(h^{4.35})$ and $O(h^{3.40})$ for IRBF4, $O(h^{8.36})$ and $O(h^{8.51})$ for IRBF6, and $O(h^{11.26})$ and $O(h^{11.34})$ for IRBF8.

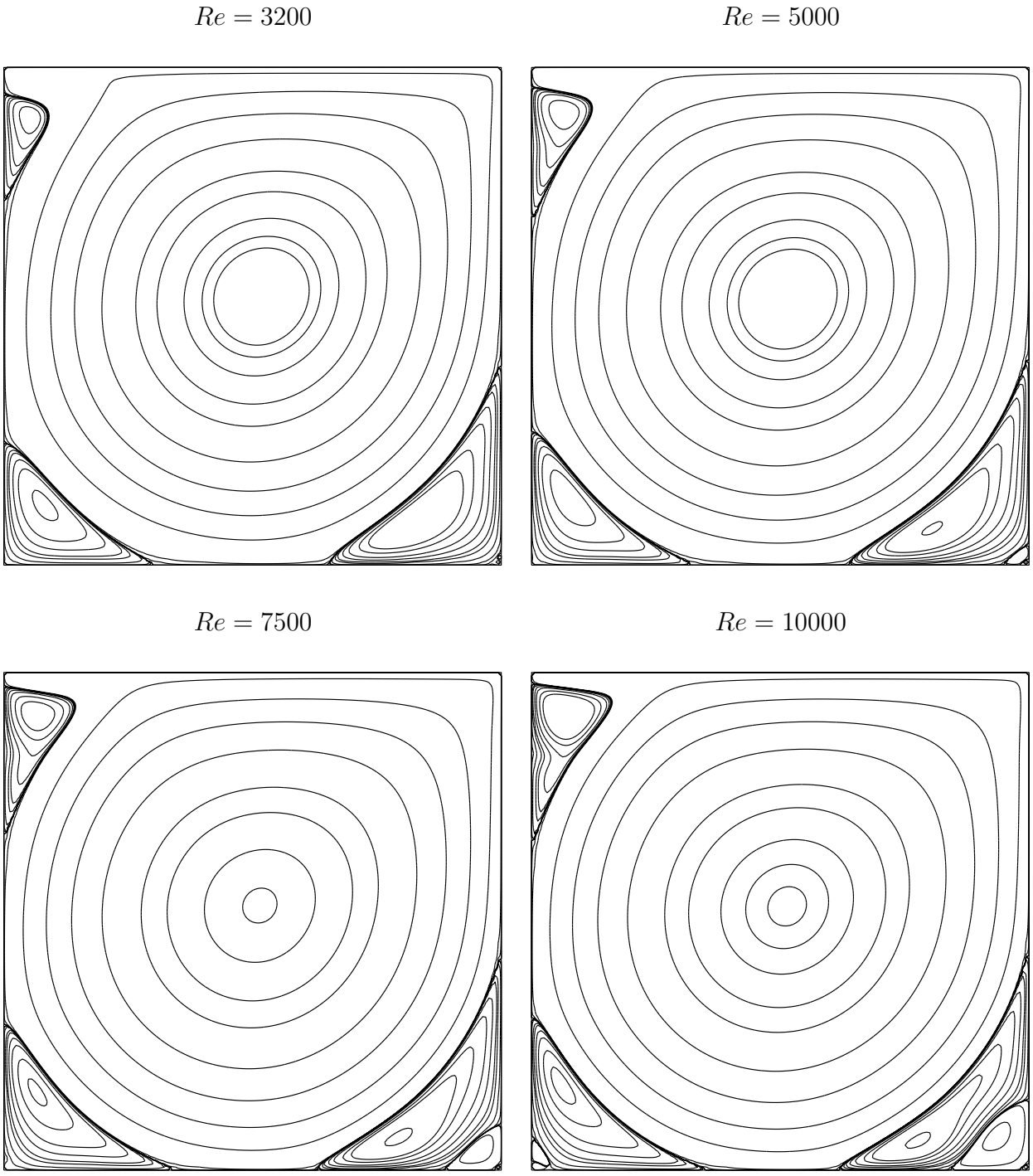

Figure 11: Square-cavity flow: Streamlines of the flow for several Re numbers using a uniform grid of 161×161.

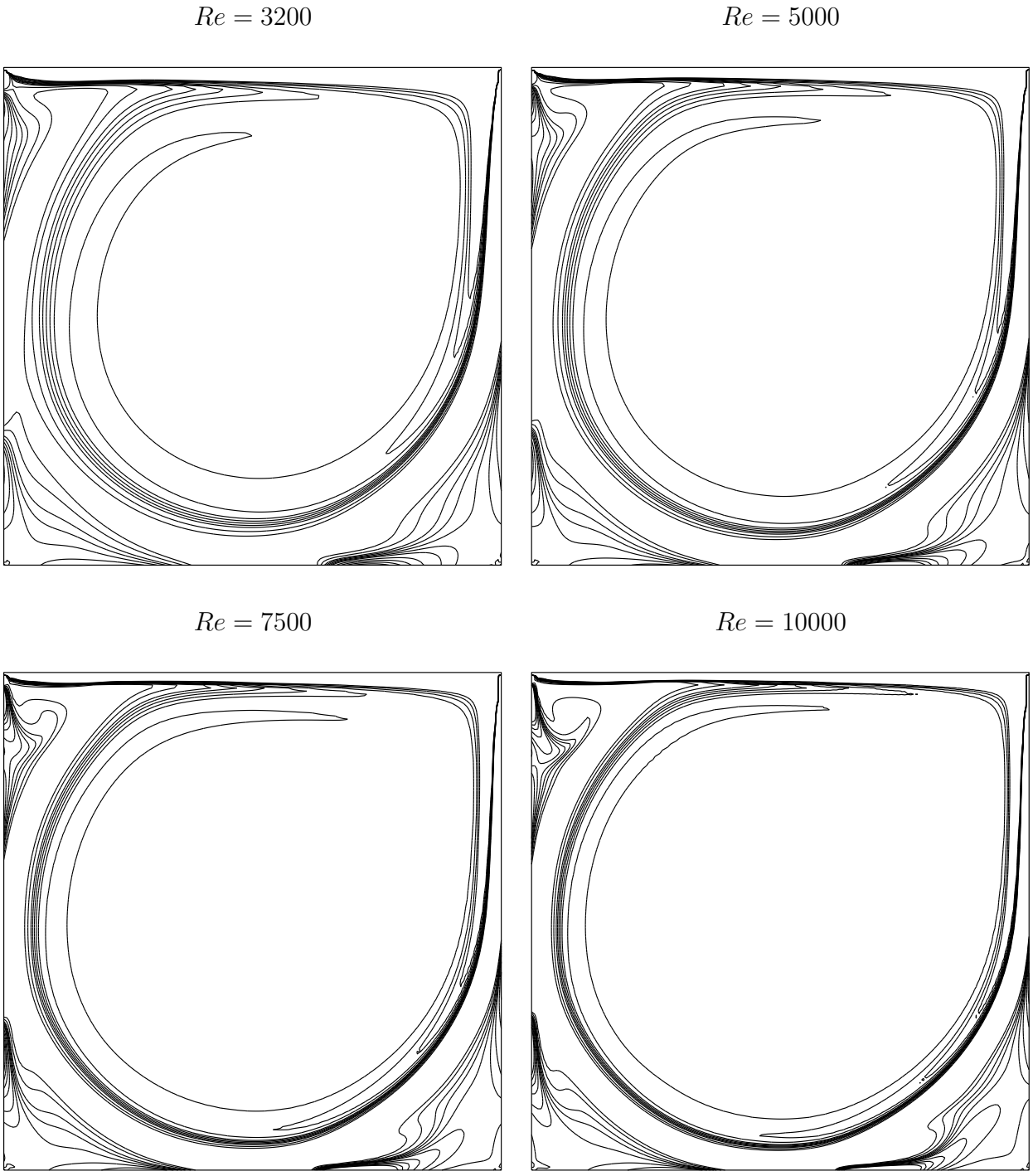

Figure 12: Square-cavity flow: Iso-vorticity lines of the flow for several Re numbers using a uniform grid of 161×161.

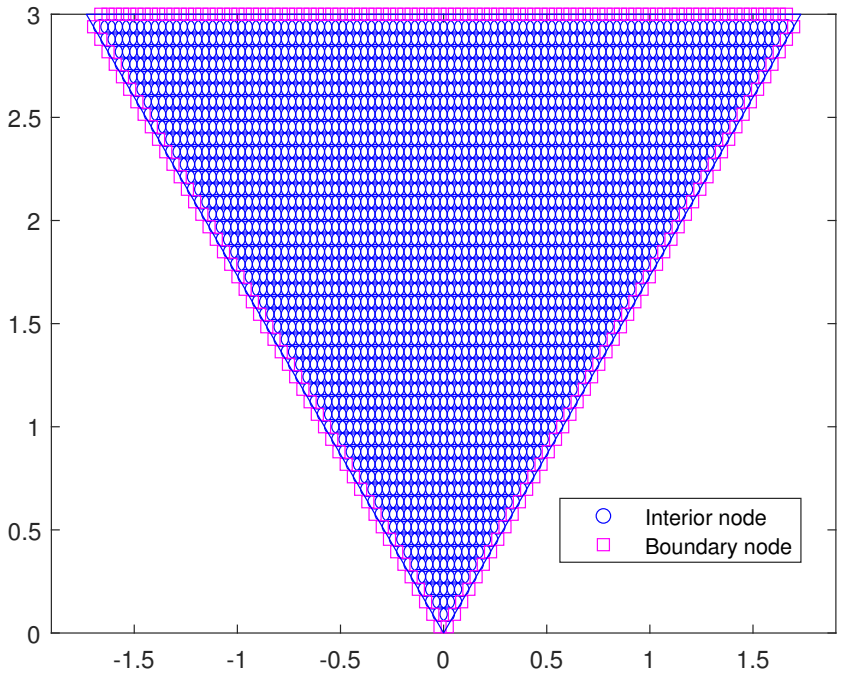

Figure 13: Triangular cavity and its associated discretisation.

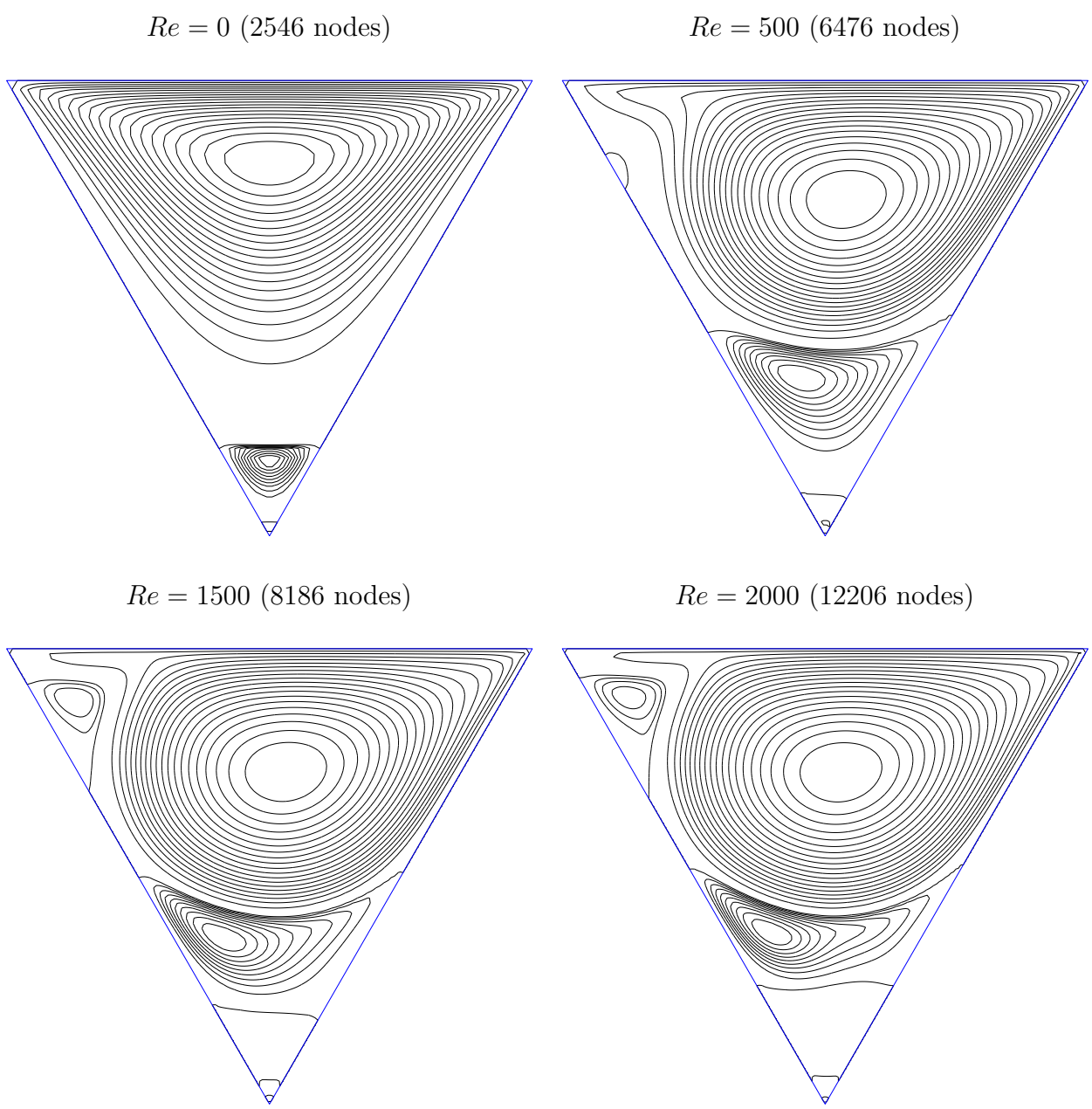

Figure 14: Triangular-cavity flow: Streamlines of the flow for several Re values. The streamline contour spacing is 0.015 for $\psi \leq 0$ and 0.0012 for $\psi > 0$.

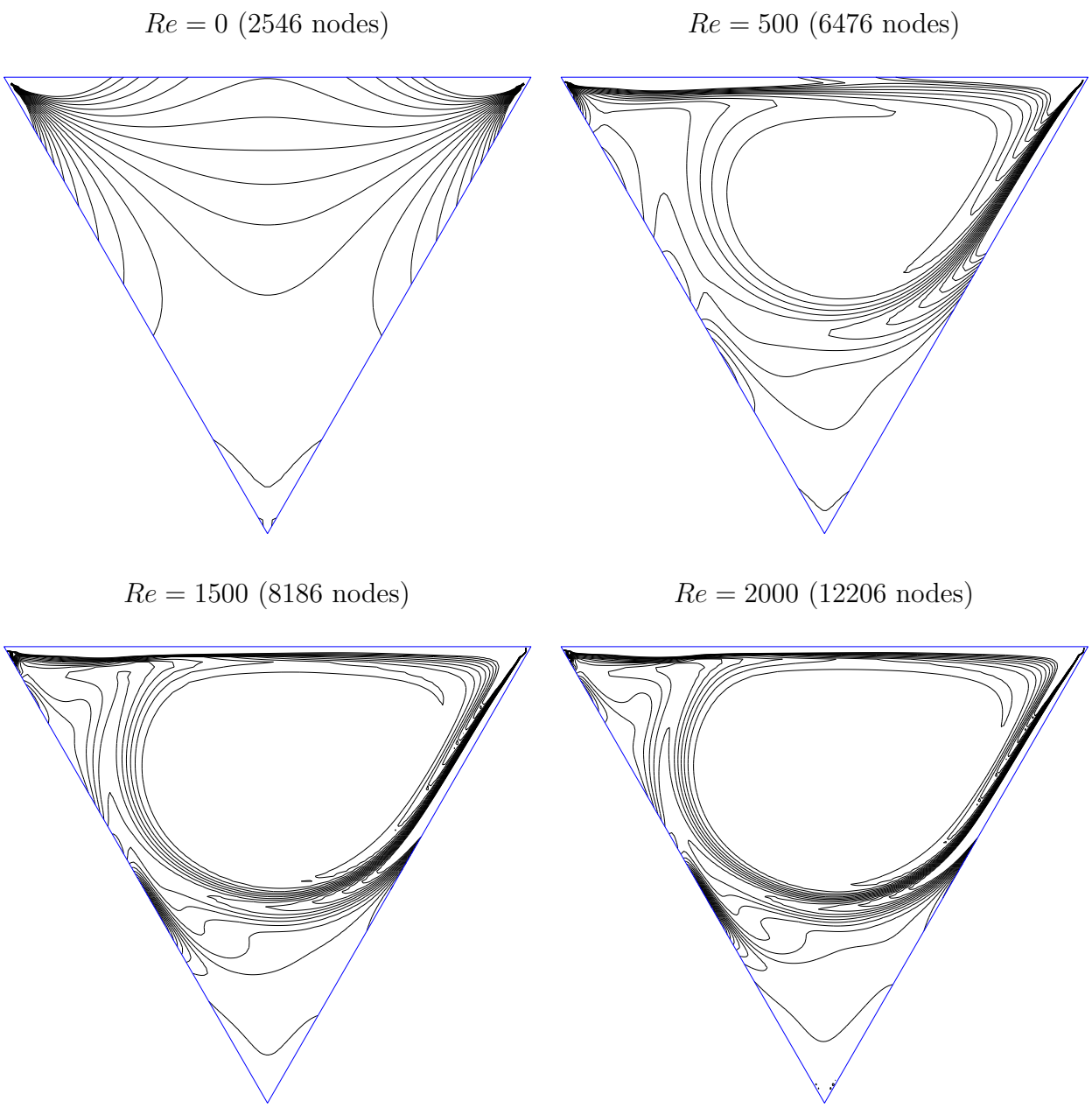

Figure 15: Triangular-cavity flow: Iso-vorticity lines of the flow for several Re values. The vorticity contour spacing is 0.5.

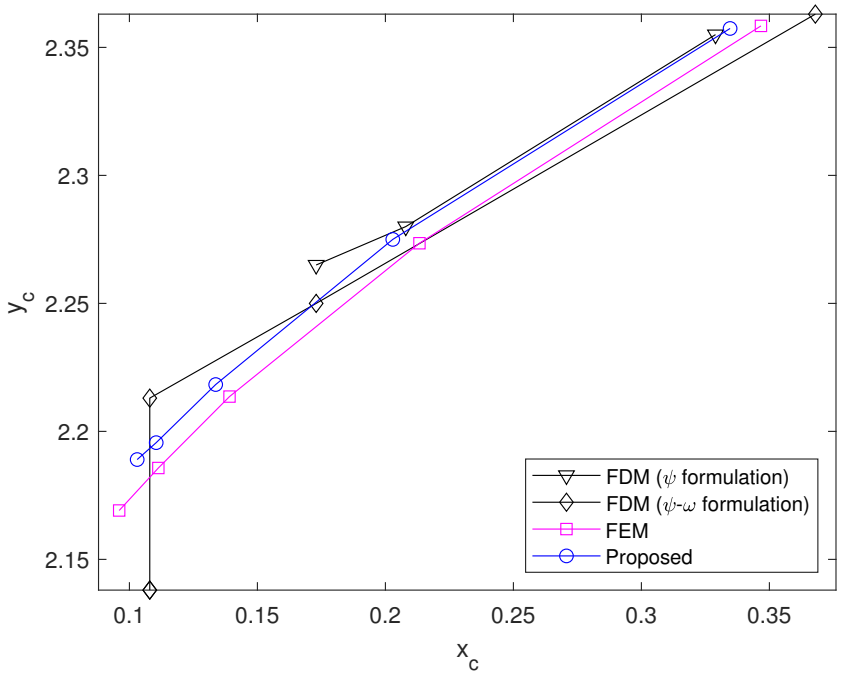

Figure 16: Triangular-cavity flow, 12206 nodes: Points from top to bottom are the centre locations of the primary eddy for the case $Re = 100$, 200, 500, 1000 and 1500, respectively.